Nanoscale

Plasmonic Heating Induced by Au Nanoparticles for Quasi-ballistic Thermal Transport in Multi-walled Carbon Nanotubes

Journal:	*Nanoscale*
Manuscript ID	NR-COM-01-2019-000901.R1
Article Type:	Communication
Date Submitted by the Author:	18-Mar-2019
Complete List of Authors:	Xu, Yanru; Wuhan University Zhao, XG; Boston University Li, Aobo; Boston University Yue, Yanan; Wuhan University Jiang, Jin; Wuhan University Zhang, Xin; Boston University, Mechanical Engineering; Boston University

Plasmonic Heating Induced by Au Nanoparticles for Quasi-ballistic Thermal Transport in Multi-walled Carbon Nanotubes

Yanru Xu[1a], Xiaoguang Zhao[2a], Aobo Li[2], Yanan Yue[1,2*], Jin Jiang[1], Xin Zhang[2,*]

[1]Key Laboratory of Hydraulic Machinery Transients (MOE), School of Power and Mechanical Engineering, Wuhan University, Wuhan, Hubei 430072, China

[2]Department of Mechanical Engineering, Boston University, Boston, Massachusetts 02215, USA

[a]These authors contribute equally

[*] E-mail: Y.Y. : yyue@whu.edu.cn; X.Z. : xinz@bu.edu

Abstract

The plasmon resonances of nanostructures enable wide applications from highly sensitive sensing to high-resolution imaging, through the improvement of photogeneration rate stimulated by the local field enhancement. However, quantitative experimental studies on the localized heating and the thermal transport process in the vicinity of plasmonics are still lacking because of the diffraction limit in conventional optothermal methodologies. In this work, we demonstrate an approach based on Raman thermometry to probe the near-field heating caused by plasmonics. An Au nanoparticles (AuNPs) array fabricated by template-assisted method is used to generate near field effect. Multi-walled carbon nanotubes (MWCNTs) dispersed on the AuNPs are employed to quantify the near-field heating from their Raman peak shifts. Results show that temperature rise of MWCNTs on AuNPs is much higher than that of a control group under the same laser irradiation. Further analysis indicates that enhanced photon absorption of MWCNTs attributed to plasmon resonances is partially responsible for the different heating effect. The non-uniform thermal hot spots at nanoscale could result in quasi-ballistic thermal transport of phonons in MWCNTs which is another reason for the temperature rise. Our results can be used to understand plasmonic heating effects as well as to

explore quasi-ballistic thermal transport in carbon-based low-dimensional materials by tailoring the geometry or size of plasmonic nanostructures.

Keywords: Raman thermometry, plasmonic heating, ballistic, carbon nanotubes, Au nanoparticles.

Introduction

Plasmon resonances of nanostructures excited by laser irradiation exhibit extraordinary local field enhancement, which are extensively used to improve the photogeneration rate of optical processes, enabling a wide range of applications ranging from highly sensitive sensing to high-resolution imaging.[1-3] Simultaneously, the confined electromagnetic field of plasmonic structure also induces significant light absorption and manifesting heating on the surrounding medium, which involves plenty of applications.[4] For example, the enhanced optical field of metallic nanoantennas in a heat-assisted magnetic recording (HAMR) system can be used to heat the medium to hundreds of degrees for efficient magnetic writing.[5] Besides, the heating of plasmonic effect via the damping of plasmon oscillation promises a variety of novel applications including photo-induced water vaporization,[6, 7] photon energy conversion,[8, 9] visible-light photocatalysis[9, 10] and laser nanofabrication.[11] The quantitative study of thermophysical properties is essential to the exploration and utilization of localized heating effect.

Theoretical calculations and numerical simulations have been conducted to study the plasmonic heating of nanostructures.[12-14] Gold-based nanoparticles (AuNPs),[15] nanostars,[16] and nanowires[17] are demonstrated to exhibit the plasmonic heating effect in many numerical studies. The titanium nitride (TiN) and zirconium nitride (ZrN) NPs are also ideal candidates for HAMR because of the stability at high temperature.[18] Array of AuNPs on substrate advances in forming localized nanoscale heating compared with those dispersed in solutions.[19] The diabolo antenna is more favorable for nanoscale heat generation compared with bow-tie structures.[20] The incorporation of antenna into a plasmonic lens has been demonstrated as a complementary structure for yielding enhanced thermal hot spots by five times.[20] The nano-gap between gold tip and substrate

could lead to a temperature rise three orders of magnitude higher than that of the substrate without the tip.[21] Besides, the near-field heating of tip-substrate cavity may bring material deformation to the substrate.[22] To manage and explore the plasmonic heating, especially for structures at nanoscale, experimental validation is in urgent need for understanding and then controlling the plasmonic heating and nanoscale heat generation.

Experimental works of nanoscale heat generation due to the plasmonic heating effect are not as many as simulations since the thermal characterization is challenging due to the intrinsic property of measurement principles. The conventional optical techniques such as infrared thermometer are limited by the diffraction effect of light. The accurate characterizations of localized temperature and plasmonic heat intensity are difficult and critical issues. Previously, the bolometric approach,[17] photoluminescence approach[20] and plasmonic absorption band[23] have been employed in thermal characterizations of gold nanostructures, while suffering from the uncertainties induced by material emissivity, intensity fluctuation or complex calibration process. Development of novel thermometry techniques at nanoscale is very much in demand for understanding the thermophysical processes under plasmonics effect. Strong photogeneration from plasmonic structures also yield Raman enhancement, known as surface enhanced Raman scattering. For a decade, Raman spectroscopy has been used as a powerful tool for thermal characterization of carbon based low-dimensional materials, such as carbon nanotubes (CNTs)[24-26] and graphene.[27-29] The resolution of Raman thermometry mainly depends on the size of probed materials or the laser spot. If the size of the target material is smaller than the laser spot size, and there is only one sample within the spot, Raman thermometry is capable of characterizing thermal properties of such a structure. [30] Thus, it could break the diffraction limit from this point of view.

With the advanced miniaturization and increased power density in electronic devices, the excessive heat has to be removed to reduce local high temperature induced by hotspots for safe and reliable operations.[31] CNTs provide an exciting opportunity for thermal management, which can be used as one-dimensional heat spreader connecting the hotspot and the heat sinks.[32] As high-thermal conductivity nanomaterials, CNTs are promising in next generation electronic applications. Temperature dependent Raman scattering and thermal property of CNTs based materials have been studied in our previous work.[33, 34] CNTs feature strong Raman signals and provide the opportunity for validating the plasmonic heating as characterization material. In addition, enhancement of Raman signals induced by plasmon resonance would provide a better thermal resolution of Raman thermometry, because the enhanced signal would result in lower noise in data processing. In this work, the AuNPs array is fabricated to generate plasmonic effect and the multi-walled CNTs (MWCNTs) are dispersed on top of the AuNPs array. The surface enhanced Raman thermometry is employed to probe the local temperature and thermal transport in MWCNTs under plasmonic heating.

Results and Discussion

Experimental and simulated optical enhancement

For easy application of Raman thermometry, the AuNPs array is patterned on a silicon substrate. Template-assisted lithography based on ultrathin alumina membrane (UTAM) is employed in the fabrication of AuNPs combined with thermal evaporation method (see Experimental Section for details).[35, 36] The SEM inset in Fig. 1a shows that AuNPs are arranged in a hexagonal array. The average diameter and periodicity of AuNPs are 30.2 ± 4.1 nm and 64.6 ± 2.4 nm, respectively. By comparing Raman signal of Si-band between AuNPs/Si

and bare Si, Raman enhancement factor of AuNPs is obtained.[2] From the experimental results (Fig. 1a), it is found that under the excitation of a 532 nm diode laser, Raman signal of Si-band can be enhanced by 18% even the large area of silicon is covered by AuNPs. Enhanced Raman scattering of patterned silicon with respect to bare silicon has been validated that it is attributed to the surface plasmon property of metallic nanostructures in Lorite et al' work[37] and our previous work.[38] The simulated extinction spectrum of AuNPs exhibits a plasmon band in the range of 400 nm to 800 nm with a peak wavelength at 554 nm and agrees well with the measured results of gold nanoparticles with similar size (see Supporting Information Section 2 for details).[39] Therefore, the plasmon property of the AuNPs could be validated in combination with Raman enhancement measurement.

For further understanding the distribution of optical enhancement, electromagnetic intensity around AuNPs is simulated (see Experimental Section for details). The diameter and the periodicity of AuNPs are important parameters in the simulation models. The effects of their deviations on the calculated electric intensity enhancement are evaluated and they are found to be negligible (see Supporting Information Section 3 for details). The results (Fig. 1b) reveal that the AuNPs exhibit a resonant response with a peak wavelength of 560 nm. At the experimental wavelength (532 nm), the overall enhancement factor for electric intensity is 2.2. The calculated Raman enhancement factor (the second power of the electric intensity enhancement factor)[40] is 4.8. It is simulated that 10～50% defects in AuNPs array may cause a reduction of 8～44% in Raman enhancement factor (see Supporting Information Section 3 for details). And the experimental values represent averaged effects over the laser focal spot region which is significantly larger with respect to the size of AuNPs. Therefore, the calculated Raman enhancement factor higher than the experimental value is

reasonable if taking the imperfection in the AuNPs array into account. The simulation results (the inset of Fig. 1b) show that owing to the excitation of plasmonic effect around AuNPs, the electric field in the vicinity of AuNPs are strongly confined within a few nanometers and distribute nonuniformly at the surface, which make the incident and scattered field amplified resulting in an enhancement in silicon Raman peak strengths.[40]

Temperature rise in MWCNTs induced by plasmonic heating

MWCNTs dispersed on a silicon substrate coated with AuNPs acts as characterization target while the bare silicon region without coating acts as the control group. For consistency of measurement, the sample (MWCNTs/AuNPs/Si) and control group (MWCNTs/Si) is on the same silicon piece. SEM images (Fig. 2a, b) of the sample and the control group show that MWCNTs (estimated diameter from 15 to 40 nm, length: 10 μm) agglomerate and distribute randomly on the substrate due to the van der Waals forces.[41] This agglomeration results in a nonuniform thickness distribution in MWCNTs layer and may cause experimental uncertainties in Raman signals if treated improperly (see Experimental Section for details). For comparison, the measurements need to be conducted on spots of the sample and control group with similar thickness of MWCNTs. Before the heating experiment, these spots are confirmed in advance. In Fig. 2c, the higher baseline of Raman spectrum from the sample stems from the fluorescence background of AuNPs and is subtracted in the data processing.[42] It is found that Raman spectrum of the control group includes Si-band (520 cm^{-1}), D-band (defects and disorder of the MWCNTs structure, 1347 cm^{-1}), G-band (close to graphite mode, 1586 cm^{-1}) and 2D-band (second-order harmonic, 2700 cm^{-1}) of MWCNTs. The D-band, G-band and

2D-band of the sample all shows redshift (lower than 3 cm^{-1}), with respect to the control group,[42] indicating that the charge transfer between MWCNTs and AuNPs is weak which makes a minor contribution to the Raman enhancement.[43] Moreover, the intensity ratio of D-band to G-band (I_D/I_G) and the ratio of D-band to 2D-band (I_D/I_{2D}) are 1.19 and 4.19, respectively, close to those of the control group (1.20 and 4.14, respectively). It means that the presence of AuNPs does not cause new defects as well as structural changes in MWCNTs.[44]

The peak intensity of D-band and G-band exhibits negligible variations from 302 K to 363 K,[45] while their peak positions shift with temperature (Fig. 3a and inset of Fig. 3b). Among the different bands of MWCNTs, D-band has the strongest intensity and is used as the temperature indicator. Its temperature coefficient is characterized as –0.02 cm^{-1} K^{-1} (Fig. 3b) in the calibration experiment, agreeing well with the literature values (–0.017~–0.019 cm^{-1} K^{-1}).[45, 46] In laser heating experiment, different power of the laser is irradiated on the same spot of the sample and the control group. The peak shift of D-band as a function of laser power is shown in Fig. 3c. As the laser intensity is increased, D-band of MWCNTs shows redshift for both the sample and the control group. The slope of D peak shift to the laser power is –0.0139 cm^{-1} mW^{-1} for the sample, which is ~3 times of the control group (–0.0044 cm^{-1} mW^{-1}). Based on the calibration results, the temperature rise in MWCNTs under different laser power is obtained. As shown in Fig. 3d, when power is increased from 12 mW to 30 mW, MWCNTs in the control group shows a small temperature rise (less than 6.6 ± 2.0 K). However, the temperature rise of MWCNTs in the sample is obviously higher over the same laser power range and its maximum value is about 20.7 ± 3.6 K. The monitored MWCNTs are both from the same batch and have similar structural distributions. Considering that the laser spot is large enough that the

measured heating effects are a general description of thermal transport through CNTs. The temperature rise difference between the sample and the control group is attributed to two aspects: 1) the enhanced photon absorption generated by the plasmonic AuNPs, and 2) lower thermophysical properties of MWCNTs on AuNPs/Si.

The temperature rise due to photon absorption enhancement can be calculated as $\Delta T_{\mathrm{CNTs}} = s * M * P$, where *s* is the slope between temperature rise of MWCNTs in the control group and laser power (0.22 K mW^{-1}) due to the pure laser heating effect on MWCNTs (Fig. 3d), *M* is the photon absorption enhancement factor and *P* is laser power, 30 mW. Enhanced photon absorption in MWCNTs is proportional to the electric intensity enhancement depending on its physical definition.[19, 47] The electric intensity enhancement around MWCNTs can be estimated from Raman experiments. Raman enhancement of MWCNTs is mainly attributed to the plasmonic AuNPs which has been confirmed in Bäuml et al' work for polarized surface-enhanced Raman measurements of suspended CNTs on Pt-Re nanoantennas.[48] As shown from Raman enhancement of our AuNPs array (Fig. 1a), the average electric intensity enhancement is around 1.09 (the root of Raman enhancement 1.18).[40]. ΔT_{CNTs} is calculated as 7.2 K. If we use the value of simulated electric intensity enhancement factor (~2.2), the corresponding temperature rise is 14.5 K, which is the upper limit since the factor is from perfect pattern without defects. The temperature rise due to the absorption enhancement (7.2~14.5 K) is smaller than the AuNPs-assisted heating effect (20.7 K), indicating that photon absorption enhancement is partially responsible for the temperature rise difference of MWCNTS between the sample and the control group.

Minimized heating effects on AuNPs and Si substrate

Before analyzing thermal transport in MWCNTs and exploring the thermophysical properties of MWCNTs, laser heating effects on AuNPs and Si substrate should be studied in advance. The heat generation in AuNPs via the plasmon decay is expressed by the enhanced light absorption[6], providing a way to analyze theoretical temperature rise in AuNPs array. The thermal transport around AuNPs (if any) is complex considering the thermal contact with silicon substrate and surrounding air. In this work, we roughly estimate the value based on a theoretical model proposed by Baffou et al.[19] The model is for a periodic array of plasmonic NPs located at the interface between two homogeneous media to simplify the reported numerical method,[15] and has been validated by temperature measurements on AuNPs. In this model, the temperature rise (ΔT) in an AuNP is expressed by $\Delta T = \Delta T_s + \Delta T_{ext}$, where ΔT_s represents the temperature rise confined at the vicinity of each NP due to the self-heating and ΔT_{ext} represents the smooth temperature profile throughout the array due to the accumulated effect from neighboring AuNPs.

ΔT_s is given by $\Delta T_s = q_{Au}(4\pi\bar{k}R)^{-1}$, where $\bar{k} = 0.5(k + k_s)$ is the mean thermal conductivity of the media in the vicinity of AuNP. k is the thermal conductivity of silicon, 148 W (m K)$^{-1}$ and k_s= 0.026 W (m K)$^{-1}$ for air. The utilized mean thermal conductivity is 74.013 W (m K)$^{-1}$. R is the equivalent radius of AuNP.[15] q_{Au} is the absorbed power in an AuNP, obtained by integration of simulated power absorption per unit volume ($\dot{q}_{Au}$) (see Supporting Information Section 1 for details). The results of $\dot{q}_{Au}$ (Fig. 4a-c) indicate that its magnitude is almost uniform throughout the whole NP, with a mean value of ~1.25×10^{14} W m^{-3}. Based on calculated q_{Au} (1.76×10^{-9} W), ΔT_s in an AuNP is estimated as 1.3×10^{-4} K which means that the self-heating in AuNP is negligible. ΔT_{ext} is expressed by $\Delta T_{ext} \approx q_{Au}D(1 - 2A^{0.5}\pi^{-0.5}D^{-1})(4\bar{k}A)^{-1}$, where D is the

diameter of laser focal spot (50 μm), and A is the effective area of one unit-cell periodicity given by $A = \sqrt{3}p^2/2$ and p is the value of one periodicity (65 nm). The value of ΔT_{ext} is calculated as 0.1 K. The heating effect accumulated from adjacent AuNPs could be assumed negligible.

In order to evaluate laser heating effect on silicon substrate, Raman measurements are performed on silicon substrate in the sample and the control group from 12 mW to 30 mW. Each spectrum is collected at least five times for averaging. The variations of Raman frequency shift with laser power are shown in Fig. 4d. Temperature coefficient of Si-band is determined by Raman calibration over a temperature range from 294 K to 364 K (see Supporting Information Section 4 for details), which is fitted as –0.023 cm^{-1} K^{-1} (see Fig. 7b), agreeing well with the reported values (–0.0201~–0.0247 cm^{-1} K^{-1}).[49-51] Fig. 4d shows that Raman peak shift of Si-band does not significantly vary with laser power. The temperature rises of silicon substrate for the sample and the control group are both below 1.3 K, which are negligible. The used maximum laser intensity here is only 0.015 mW μm^{-2}, two orders of magnitude lower than the threshold value (2.5 mW μm^{-2}) for producing observable temperature rise in bulk silicon.[52] Thereby, the temperature rise in AuNPs and silicon substrate is negligible. Meanwhile, we could deduce that the AuNPs and silicon substrate can act as perfect heat sinks for MWCNTs which contact either AuNPs or silicon substrate.

Thermal transport in MWCNTs

SEM image of MWCNTs (Fig. 2b) shows that there is a large number of contact points in the MWCNTs agglomeration. Thermal transport across these MWCNTs junctions plays a critical role in the collective heat transfer through MWCNTs agglomeration,[53-55] which is relevant to various geometrical[56], structural[57] and

external parameters[58] and is extremely complicated. In order to analyze and compare the thermal property of MWCNTs between the sample and the control group, a simplified model is used to describe the complex heat transfer through MWCNTs. Under the compensative effect of various internal and external factors, MWCNTs agglomeration is regarded as a one-dimensional MWCNT composite. The temperature rise measured by Raman thermometry is regarded as the average temperature rise in this one-dimensional substitute. In practice, to support the material, the ends of such composite are always in thermal contacts with the silicon substrate or AuNPs. Since the temperature rise of AuNPs and silicon substrate are evaluated negligible. Therefore, the temperature at the ends of the composite is room temperature. Heat generated inside the one-dimensional composite is transferred along the axial direction, as shown in Fig. 5a, b. Therefore, the one-dimensional steady-state model is applicable.

The mean temperature of MWCNT composite is evaluated from:[34] $\overline{T} = \overline{\dot{q}_C} L^2 (3k)^{-1} + T_0$, where $(\overline{T} - T_0)$ is the mean temperature rise, directly obtained from experimental results in Fig. 3d, L is the half length of MWCNT (5 μm), k is the thermal conductivity, and $\overline{\dot{q}_C}$ is the mean heat generation per unit volume deduced from the photon absorption in MWCNTs which is estimated by $\overline{\dot{q}_C} = P_0 \alpha M r_t r_0^{-2} A_C^{-1}$, where P_0 (30 mW) is the laser energy, r_t (15 nm) is the radius of MWCNT, measured from Fig. 2b, A_C is the cross section area, r_0 is the radius of laser focal spot, M is the mean electric field intensity enhancement factor (1.09 for near field enhancement of AuNPs, and 1 for bare silicon), α is the laser absorptance: 0.037, estimated based on reported values for the MWCNTs with similar structure and incident wavelength.[59] The equivalent thermal conductivity of MWCNT is calculated by solving above equation as 47 W (m K)$^{-1}$ for the one on bare silicon (control group) and 16 W (m K)$^{-1}$ for on AuNPs/Si, respectively. They are apparent values, since the thermal

resistance of numerous CNT junctions, the value of calculated thermal conductivity are both small and much lower than that of a single suspended MWCNT.[60]

Compared with the control group, equivalent thermal conductivity of MWCNTs on AuNPs is suppressed by 66%, though the MWCNT sample is from the same batch and all other experimental conditions are the same. To explore the origin, the mean free path of phonons in MWCNTs is roughly estimated by $l \approx k(C_v v)^{-1}$ based on the kinetic theory.[61] Assuming C_V as 629.8 kJ (m^3 K)$^{-1}$, v the sound velocity of MWCNTs as 10^4 m s^{-1}, the phonon mean free path of the control group is estimated to be 7 nm. It is mentioned above that the length dimension of the region confining the electromagnetic field is about 6 nm along the *x* axis and 28 nm along the *y* axis, as shown in the inset of Fig. 1b. The size of hot spots is just comparable to the calculated mean free paths of phonons. Therefore, the localized thermal transport may become quasi-ballistic which would greatly reduce thermal conductivity of MWCNTs.[62] Additionally, as shown in the inset of Fig. 1b, the hot spots distribute non-uniformly across the layer of AuNPs, leading to non-uniform heating on MWCNTs and thus resulting in nonequilibrium of phonon transport from randomly distributed hot spots and also causing reduction in thermal conductivity of MWCNTs, which is another reason for the higher temperature rise observed in the sample. Current study is conducted at low laser energy levels, more significant temperature difference could be observed if AuNPs are exposed to much more intense laser energy below 31.4 W on the premise that AuNPs could not be damaged.[63]

Conclusions

We characterize the plasmonic heating effect of a two-dimensional AuNPs array on MWCNTs and find that

the temperature rise of MWCNTs under plasmonic heating is about two times higher than the same materials on bare silicon under the same levels of laser energy irradiation. The large difference in temperature rise is partially attributed to the enhanced photon absorption of MWCNTs as validated by the enhanced Raman signal due to the plasmon resonances of AuNPs. In addition, the nanoscale hot spots at the top surface of AuNPs result in quasi-ballistic phonon transport inside MWCNTs and the reduction of phonon mean free path lowers the thermal conductivity of MWCNTs. This work offers a feasible way for thermal characterization in near field based on Raman thermometry. Meanwhile, our results are beneficial for understanding near-field heating effect as well as quasi-ballistic thermal transport in low-dimensional materials.

Experimental Section

Fabrication of AuNPs array: The array of AuNPs is fabricated through template-assisted lithography based on ultrathin alumina membrane (UTAM), which has been demonstrated to be an effective way for patterning well-defined NPs. The template is a 200-nm-thick commercialized UTAM that has self-organized honeycomb-like nanopores with an average diameter of 45 nm and a periodicity of 65 nm. The UTAM layer is supported by a layer of polymethyl methacrylate (PMMA). Sample fabrication processes are illustrated in Fig. 6. PMMA/UTAM is first transferred to a silicon substrate [(100), p-type doping]. Then, the cover is removed by acetone baths, leaving only UTAM on silicon. By using thermal evaporation, 20 nm of Au (99.99%) film is deposited on UTAM/Si with a 5 nm adhesion layer of Cr (99.99%), under high vacuum ($2.7\text{─}2.8\times10^{-4}$ Pa) with an evaporation rate of 0.03─0.08 nm s^{-1}. After lift-off, the AuNPs array is patterned on a silicon substrate (hereafter AuNPs/Si). The plasmon-induced enhancement is confirmed by Raman

characterization of AuNPs/Si and bare Si under the excitation of a 532 nm diode laser.

Simulation details: Electromagnetic field distribution around the AuNPs array is simulated by using finite-difference time-domain (FDTD) method.[64] Details of the simulation can be found in the Supporting Information Section 1. The electric intensity enhancement factor is calculated by averaging the second power of field enhancement which is represented as the ratio of the local electric field (E_{loc}) to the incident electric field (E_0, 1 V m^{-1}). The numerical model for calculating the power absorption per unit volume in AuNPs is the same as that described in the Supporting Information Section 1. The input incident electric field is corresponding to the used laser intensity of 0.015 mW μm^{-2}.

Fabrication of MWCNTs/AuNPs/Si and MWCNTs/Si: MWCNTs are dispersed in ethyl alcohol, treated by ultrasonication for 20 minutes, before being deposited on a silicon substrate that is partially coated with AuNPs, as shown in Fig. 6. MWCNTs/AuNPs/Si and MWCNTs/Si are characterized by using scanning electronic microscope and Raman spectrometer with a 532 nm diode laser.

Measurement setup: The schematic of laser heating experiment is illustrated in the upper inset of Fig. 2c. For the MWCNTs/AuNPs/Si sample, the plasmonic effect of AuNPs provides additional heating in MWCNTs besides the direct laser heating. As a comparison, only direct laser heating is involved in the control group. To eliminate the error caused by single data, temperature rise of MWCNTs is estimated by the fitted slope between laser power and D-band peak shift. A Raman spectrometer (B&W Tek) equipped with a 532 nm diode laser (energy adjustable) is used for exciting and collecting Raman signals and heating samples. The

laser focal spot is 50 μm in diameter and sample are illuminated by laser power from 12 to 30 mW which generates power intensities ranging from 0.006 mW μm^{-2} to 0.015 mW μm^{-2}. The integration time varies from 1.5 to 4 minutes to get strong Raman signals. To ensure the accuracy of measurement, each spectrum is collected at least five times for averaging. The peak position of D-band and Si-band are obtained by Lorentz function fitting. The locations with similar MWCNTs thickness on AuNPs/Si samples and the control group are firstly confirmed (see Supporting Information Section 4 for details). Since it is difficult to directly measure the MWCNTs thickness, we use Raman intensity of D-band to monitor MWCNTs thickness variation[65]. D-band peak intensity of the sample correlates closely with both MWCNTs thickness and Raman enhancement. By using Raman mapping (scanning), the regions with the smallest difference in D-band intensity (or silicon intensity) for the sample and the control group are labeled, as shown in Fig. 2c. The signals are recorded at an integration time of 1.5 minutes under the same focal levels. The lower inset of Fig. 2c shows that, between the MWCNTs/AuNPs/Si sample and the control group, D-band intensity differs by 5%. Considering optical enhancement generated by AuNPs, the MWCNTs at these two locations are considered at the same thickness.

Supporting Information

Supporting Information is available from the Wiley Online Library or from the author.

Acknowledgments

Y. Y. thanks the financial support from the National Natural Science Foundation of China (No. 51576145). X. Z. and X. Z. acknowledge the National Science Foundation (ECCS-1810252).

Conflict of interests

The authors declare that they have no conflict of interest.

Notes and references

1 J. Kneipp, H. Kneipp and K. Kneipp, *Chem Soc Rev*, 2008, **37**, 1052-1060.
2 P. Kusch, S. Mastel, N. S. Mueller, N. Morquillas Azpiazu, S. Heeg, R. Gorbachev, F. Schedin, U. Hübner, J. I. Pascual, S. Reich and R. Hillenbrand, *Nano Lett.*, 2017, **17**, 2667-2673.
3 Y. Shen, X. Cheng, G. Li, Q. Zhu, Z. Chi, J. Wang and C. Jin, *Nanoscale Horiz.*, 2016, **1**, 290-297.
4 J. C. Ndukaife, V. M. Shalaev and A. Boltasseva, *Science*, 2016, **351**, 334-335.
5 N. Zhou, X. Xu, A. T. Hammack, B. C. Stipe, K. Gao, W. Scholz and E. C. Gage, *Nanophotonics*, 2014, **3**, 141-155.
6 K. Setoura, S. Ito and H. Miyasaka, *Nanoscale*, 2017, **9**, 719-730.
7 C. Ma, J. Yan, Y. Huang, C. Wang and G. Yang, *Sci. Adv.*, 2018, **4**, eaas9894.
8 J. Yan, P. Liu, C. Ma, Z. Lin and G. Yang, *Nanoscale*, 2016, **8**, 8826-8838.
9 B. C. Marin, J. Ramírez, S. E. Root, E. Aklile and D. J. Lipomi, *Nanoscale Horiz.*, 2017, **2**, 311-318.
10 P. Christopher, H. Xin and S. Linic, *Nat. Chem.*, 2011, **3**, 467-472.
11 Y. Osaka, S. Sugano and S. Hashimoto, *Nanoscale*, 2016, **8**, 18187-18196.
12 G. Baffou and R. Quidant, *Laser Photonics Rev.*, 2012, **7**, 171-187.
13 A. O. Govorov and H. H. Richardson, *Nano Today*, 2007, **2**, 30-38.
14 O. Blum and N. T. Shaked, *Light Sci. Appl.*, 2015, **4**, e322.
15 G. Baffou, R. Quidant and F. J. García de Abajo, *ACS Nano*, 2010, **4**, 709-716.
16 R. Rodríguez-Oliveros and J. A. Sánchez-Gil, *Opt. Express*, 2012, **20**, 621-626.
17 P. Zolotavin, A. Alabastri, P. Nordlander and D. Natelson, *ACS Nano*, 2016, **10**, 6972-6979.
18 A. Lalisse, G. Tessier, J. Plain and G. Baffou, *Sci. Rep.*, 2016, **6**, 38647.
19 G. Baffou, P. Berto, E. Bermúdez Ureña, R. Quidant, S. Monneret, J. Polleux and H. Rigneault, *ACS Nano*, 2013, **7**, 6478-6488.
20 Z. J. Coppens, W. Li, D. G. Walker and J. G. Valentine, *Nano Lett.*, 2013, **13**, 1023-1028.
21 A. Downes, D. Salter and A. Elfick, *Opt. Express*, 2006, **14**, 5216-5222.
22 W. Zhang, T. Schmid, B. S. Yeo and R. Zenobi, *J. Phys. Chem. C*, 2008, **112**, 2104-2108.
23 O. A. Yeshchenko, N. V. Kutsevol and A. P. Naumenko, *Plasmonics*, 2016, **11**, 345-350.
24 J. H. Liu, H. H. Xie, Y. D. Hu, X. Zhang and Y. Y. Zhang, *Int. J. Heat Mass Transfer*, 2017, **108**, 572-576.
25 J. Liu, T. Li, Y. Hu and X. Zhang, *Nanoscale*, 2017, **9**, 1496-1501.
26 Q. Y. Li, K. Takahashi and X. Zhang, *Int. J. Heat Mass Transfer*, 2019, **134**, 539-546.
27 Y. N. Yue, J. C. Zhang and X. W. Wang, *Small*, 2011, **7**, 3324-3333.

28 Q. Y. Li, W. G. Ma and X. Zhang, *Int. J. Heat Mass Transfer*, 2016, **95**, 956-963.

29 Q. Y. Li, K. Xia, J. Zhang, Y. Zhang, Q. Li, K. Takahashi and X. Zhang, *Nanoscale*, 2017, **9**, 10784-10793.

30 H. D. Wang, J. H. Liu, Z. Y. Guo, X. Zhang, R. F. Zhang, F. Wei and T. Y. Li, *Nanoscale Microscale Thermophys. Eng.*, 2013, **17**, 349-365.

31 L. Qiu, P. Guo, X. Yang, Y. Ouyang, Y. Feng, X. Zhang, J. Zhao, X. Zhang and Q. Li, *Carbon*, 2019, **145**, 650-657.

32 E. F. Antunes, A. O. Lobo, E. J. Corat and V. J. Trava-Airoldi, *Carbon*, 2007, **45**, 913-921.

33 Y. Yue, X. Huang and X. Wang, *Phys. Lett. A*, 2010, **374**, 4144-4151.

34 M. Li and Y. N. Yue, *J. Nanosci. Nano Techno.*, 2015, **15**, 3004-3010.

35 A. Al-Haddad, Z. Zhan, C. Wang, S. Tarish, R. Vellacheria and Y. Lei, *ACS Nano*, 2015, **9**, 8584-8591.

36 Q. Fu, Z. Zhan, J. Dou, X. Zheng, R. Xu, M. Wu and Y. Lei, *ACS Appl. Mater. Inter.*, 2015, **7**, 13322-13328.

37 I. Lorite, A. Serrano, A. Schwartzberg, J. Bueno and J. L. Costa-Krämer, *Thin Solid Films*, 2013, **531**, 144-146.

38 X. Yanru, W. Yanqing, C. Yixin, Y. Yanan and J. Jin, *Mater. Res. Express*, 2018, **5**, 065057.

39 Z. Huang, G. Meng, B. Chen, C. Zhu, F. Han, X. Hu and X. Wang, *J. Nanosci. Nanotechnol.*, 2016, **16**, 934-938.

40 M. Moskovits, *J. Raman Spectrosc.*, 2005, **36**, 485-496.

41 A. Das, K. W. Stöckelhuber, R. Jurk, M. Saphiannikova, J. Fritzsche, H. Lorenz, M. Klüppel and G. Heinrich, *Polymer*, 2008, **49**, 5276-5283.

42 M. Scolari, A. Mews, N. Fu, A. Myalitsin, T. Assmus, K. Balasubramanian, M. Burghard and K. Kern, *J. Phys. Chem. C*, 2008, **112**, 391-396.

43 P. Corio, S. D. M. Brown, A. Marucci, M. A. Pimenta, K. Kneipp, G. Dresselhaus and M. S. Dresselhaus, *Phys. Rev. B*, 2000, **61**, 13202.

44 H. Chu, J. Wang, L. Ding, D. Yuan, Y. Zhang, J. Liu and Y. Li, *J. Am. Chem. Soc.*, 2009, **131**, 14310-14316.

45 S. Osswald, M. Havel and Y. Gogotsi, *J. Raman Spectrosc.*, 2007, **38**, 728-736.

46 F. Huang, K. T. Yue, P. Tan, S. L. Zhang, Z. Shi, X. Zhou and Z. Gu, *J. Appl. Phys.*, 1998, **84**, 4022-4024.

47 A. A. Balandin, S. Ghosh, W. Bao, I. Calizo, D. Teweldebrhan, F. Miao and C. N. Lau, *Nano Lett.*, 2008, **8**, 902-907.

48 C. Bäuml, T. Korn, C. Lange, C. Schüller, C. Strunk and N. Paradiso, *Phys. Rev. B*, 2017, **96**, 035408.

49 J. Menéndez and M. Cardona, *Phys. Rev. B*, 1984, **29**, 2051-2059.

50 H. H. Burke and I. P. Herman, *Phys. Rev. B*, 1993, **48**, 15016-15024.

51 X. Tang, S. Xu, J. Zhang and X. Wang, *ACS Appl. Mater. Interfaces*, 2014, **6**, 2809.

52 T. T. Rantala and J. Levoska, *J. Appl. Phys.*, 1989, **65**, 4475-4479.

53 V. Varshney, J. Lee, D. Li, J. S. Brown, B. L. Farmer, A. A. Voevodin and A. K. Roy, *Carbon*, 2017, **114**, 15-22.

54 Y. Yue, J. Zhang, Y. Xie, W. Chen and X. Wang, *Int. J. Heat Mass Transfer*, 2017, **110**, 827-844.

55 Q. Y. Li, K. Katakami, T. Ikuta, M. Kohno, X. Zhang and K. Takahashi, *Carbon*, 2019, **141**, 92-98.

56 Q. Rong, C. Shao and H. Bao, *J. Appl. Phys.*, 2017, **121**, 054302.

57 R. N. Salaway and L. V. Zhigilei, *Phys. Rev. B*, 2016, **94**, 014308.

58 W. Chen, J. Zhang and Y. Yue, *Int. J. Heat Mass Transfer*, 2016, **103**, 1058-1064.

59 Q. Y. Li, J. H. Liu, H. D. Wang, X. Zhang and K. Takahashi, *Rev. Sci. Instrum.*, 2013, **84**, 104905.

60 P. Kim, L. Shi, A. Majumdar and P. L. McEuen, *Phys. Rev. Lett.*, 2001, **87**, 215502.

61 D. J. Yang, Q. Zhang, G. Chen, S. F. Yoon, J. Ahn, S. G. Wang, Q. Zhou, Q. Wang and J. Q. Li, *Phys. Rev. B*, 2002, **66**, 165440.

62 T. Oyake, M. Sakata and J. Shiomi, *Appl. Phys. Lett.*, 2015, **106**, 073102.

63 K. Setoura, Y. Okada and S. Hashimoto, *Phys. Chem. Chem. Phys.*, 2014, **16**, 26938-26945.

64 A. Heltzel, S. Theppakuttai, S. C. Chen and J. R. Howell, *Nanotechnology*, 2008, **19**, 025305.

65 A. Duzynska, M. Swiniarski, A. Wroblewska, A. Lapinska, K. Zeranska, J. Judek and M. Zdrojek, *Carbon*, 2016, **105**, 377-386.

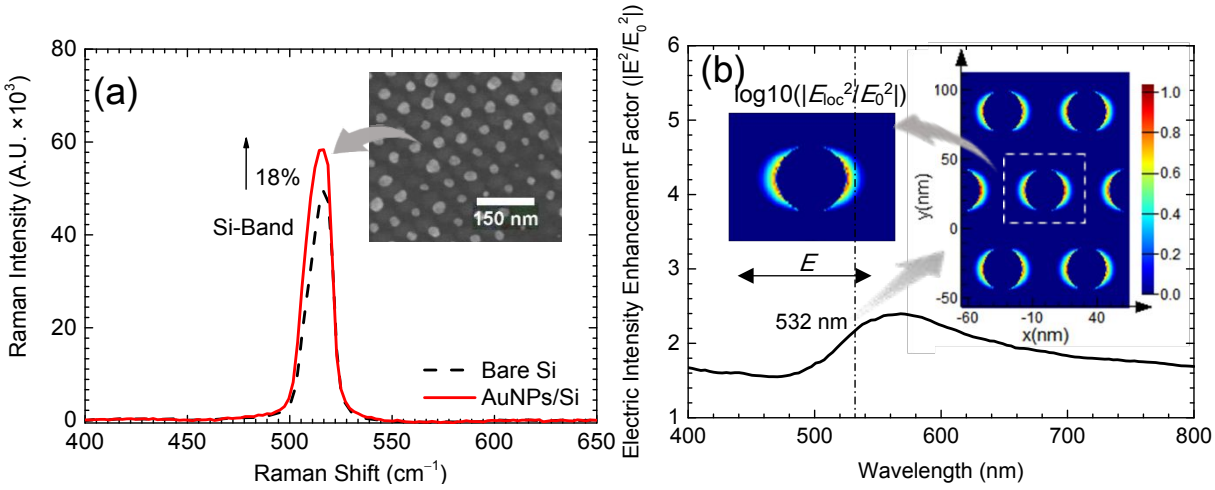

Fig. 1. (a) Raman spectra of Si-band for AuNPs/Si and bare Si. Peak intensity of Si-band is enhanced by 18% due to AuNPs. The inset depicts an SEM image of AuNPs array on the silicon substrate. (b) Calculated averaged electric intensity enhancement factor ($|E_{loc}^2/E_0^2|$) over the top surface of AuNPs as a function of incident wavelength. The insets depict the electric field intensity enhancement ($|E_{loc}^2/E_0^2|$, on a log scale) distribution on the top surface.

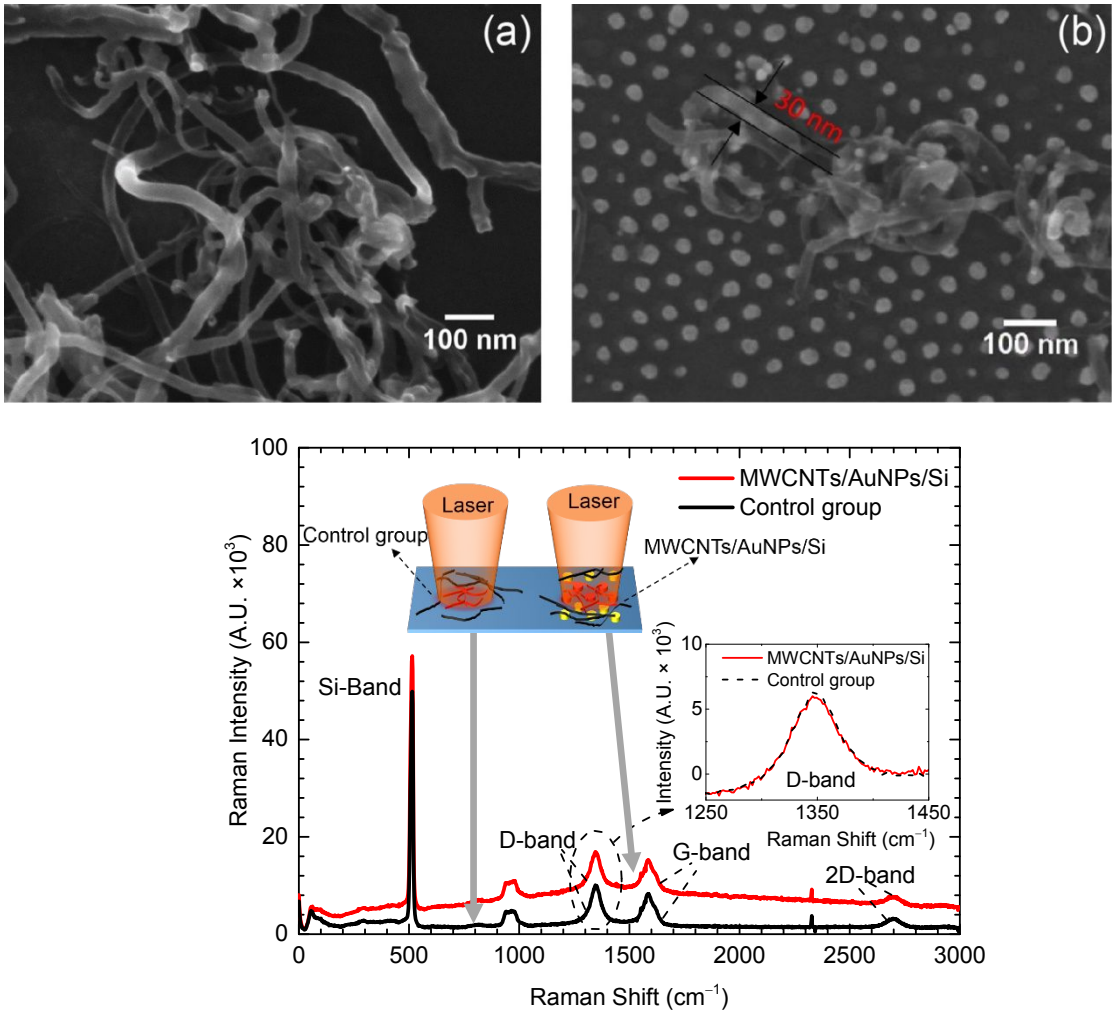

Fig. 2. SEM images of (a) MWCNTs/Si (as a control group) and (b) MWCNTs/AuNPs/Si. The diameter of individual MWCNT ranges from 15 nm to 40 nm. (c) Comparison of Raman spectra from targeting locations between sample and control group, with Si-band, D-band, G-band and 2D-band of MWCNTs. The lower inset depicts that peak intensity of D-band for the sample is similar as that of the control group. The upper inset illustrates schematic of laser heating on sample and control group by adjusting laser power.

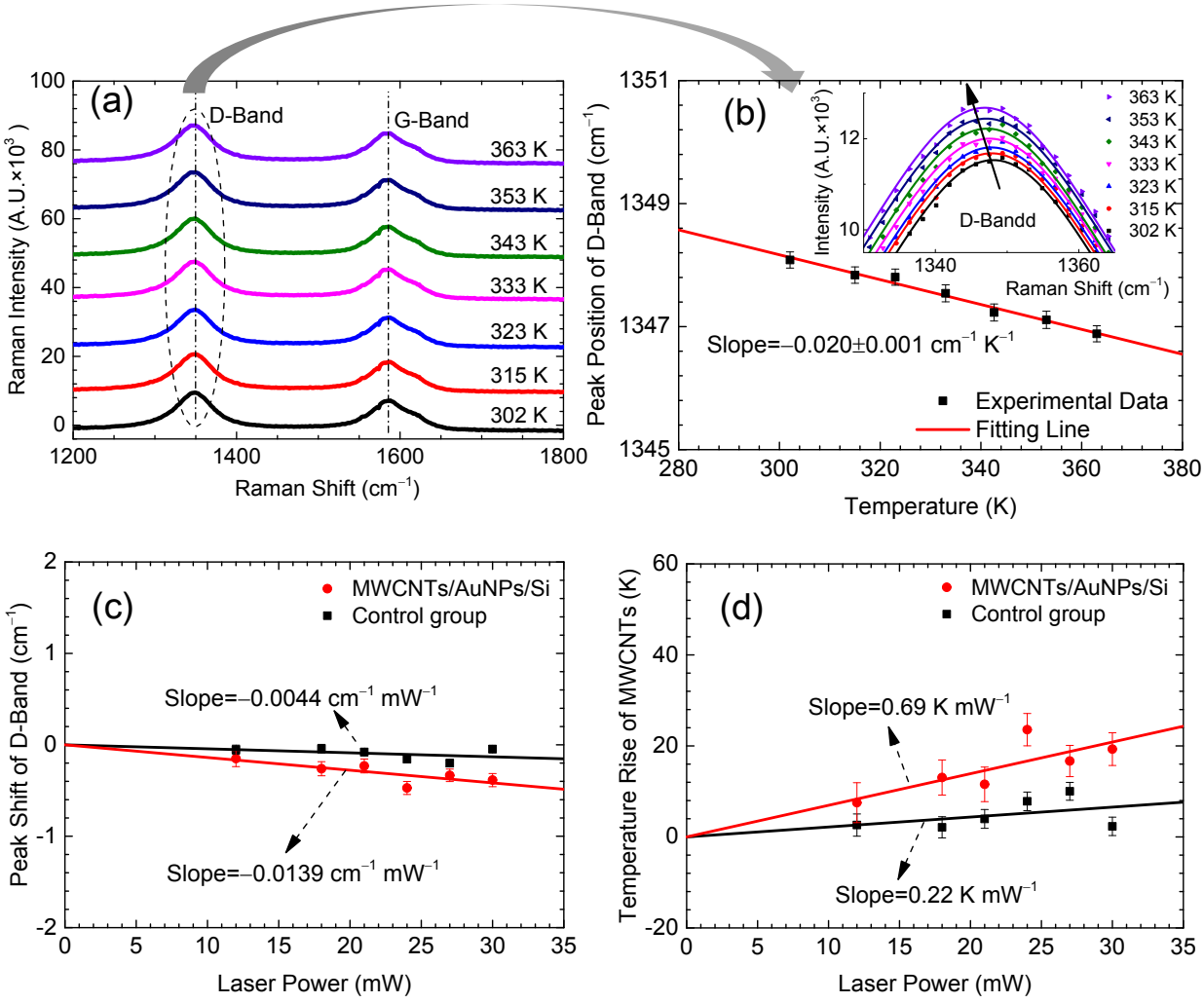

Fig. 3. (a) Raman spectrum of MWNCTs at different temperatures, with none variations in peak intensity of D-band and G-band but variations in peak positions of D-band and G-band. (b) D-band peak position as a function of temperature. The inset depicts that fitting line of D-band spectrum downshifts as temperature is increased from 302 K to 363 K. (c) D-band peak shift of sample shows linearity with laser power, with slope three times as large as that of the control group. (d) Temperature rise of MWCNTs in sample deduced based on the results in (a-c), higher than that in control group at the same laser power.

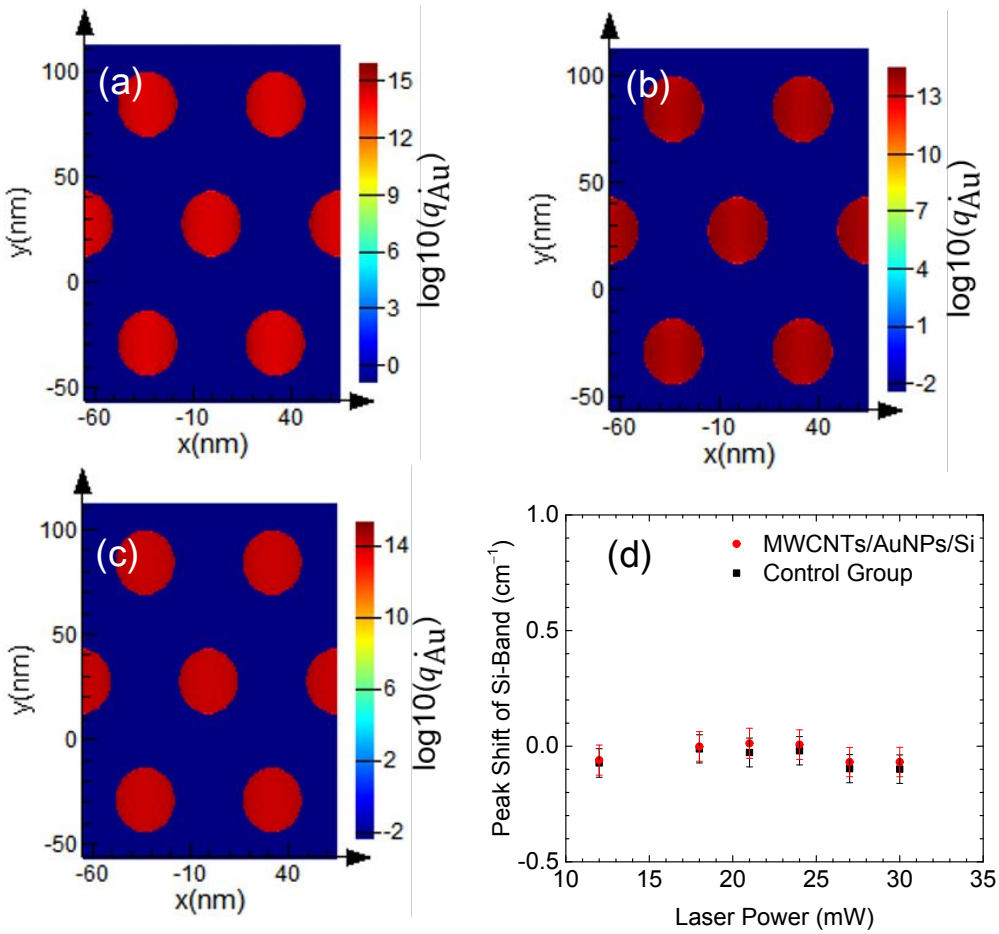

Fig. 4. The distribution of power absorption per unit volume (on a log scale) on three xy planes including (a) bottom, (b) center and (c) top surface. The average value is ~1.25×10^{14} W m^{-3} under incident laser intensity of 0.015 mW μm^{-2}. (d) Peak shift of Si-band under different laser power for sample and control group.

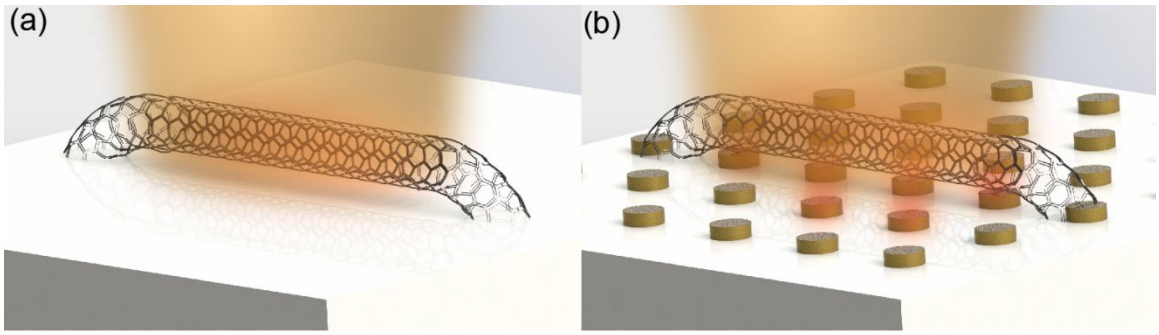

Fig. 5. The schematic of thermal transport in a single MWCNT on a silicon substrate (a) without and (b) with AuNPs along the axial direction under the irradiation of a laser beam.

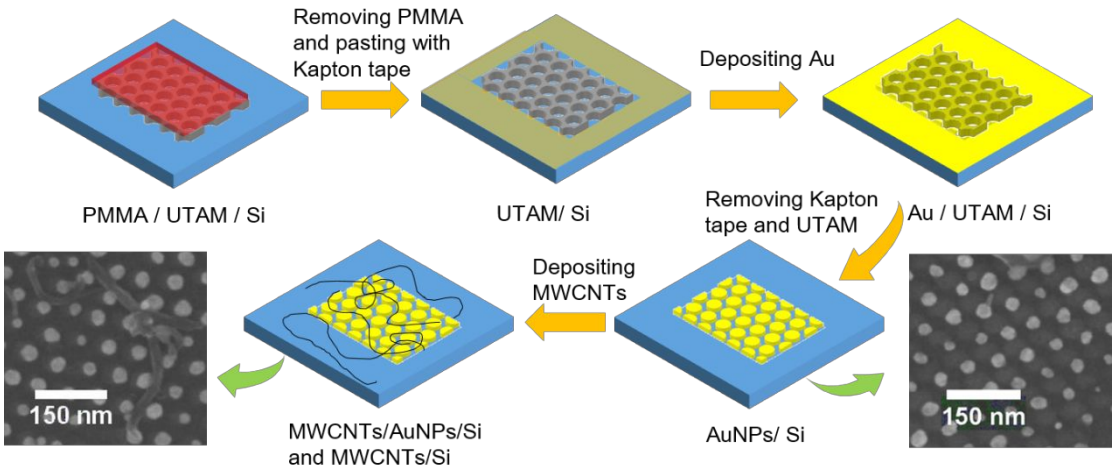

Fig. 6. The preparation processes of MWCNTs/AuNPs/Si and control group. PMMA/UTAM is carefully placed on a silicon wafer. PMMA/UTAM/Si is subsequently processed with acetone baths to remove PMMA, leaving only UTAM on silicon as a mask. The rest of the silicon substrate are covered by Kapton tape. Gold thin film is subsequently deposited on UTAM/Si by thermal evaporation. After the Kapton tape is removed, sample is placed in a sodium hydroxide solution for lift-off, leaving only AuNPs on the substrate, as shown in the right SEM inset. Dissolved MWCNTs are dribbled on silicon with and without AuNPs, as shown in the left SEM inset.